Mon. Not. R. Astron. Soc. **000**, 1–11 (2015) Printed 20 June 2016 (MN LATEX style file v2.2)

The Magnetic Field as a Turbulence Suppressor in Molecular Cloud Formation

arXiv:1606.05343v1 [astro-ph.GA] 16 Jun 2016

Manuel Zamora-Avilés,[1,2]* Enrique Vázquez-Semadeni,[2] Bastian Körtgen,[3] Robi Banerjee,[3] and Lee Hartmann[1]

[1] *Department of Astronomy, University of Michigan, 311 West Hall, 1085 S. University Ann Arbor, MI 48109-1107*
[2] *Centro de Radioastronomía y Astrofísica, UNAM. Apdo. Postal 72-3 (Xangari), Morelia, Michocán 58089, México*
[3] *Hamburger Sternwarte, Universität Hamburg, Gojenbergsweg 112, 21029 Hamburg, Germany*

Submitted to MNRAS, 20 June 2016

ABSTRACT

We present magnetohydrodynamic simulations aimed at studying the effect of the magnetic field on the production of turbulence through various instabilities during the formation of molecular clouds (MCs) by converging flows. We particularly focus on the subsequent star formation (SF) activity. We study four magnetically supercritical models with magnetic field strengths $B = 0$, 1, 2, and 3 μG (corresponding to mass-to-flux ratios of ∞, 4.76, 2.38, and 1.59 times the critical value), with the magnetic field initially aligned with the flows. We find that, for increasing magnetic field strength, the clouds formed tend to be more massive, denser, less turbulent, and with higher SF activity. This causes the onset of star formation activity in the non-magnetic or more weakly magnetized cases to be delayed by a few Myr in comparison to the more strongly magnetized cases. We attribute this behavior to a suppression of the nonlinear thin shell instability (NTSI), which is the main mechanism responsible for turbulence generation in the forming clouds, by the mean magnetic field. This result is contrary to the standard notion that the magnetic field provides support to the clouds, thus reducing their SFR. However, our result is a completely nonlinear one, and could not be foreseen from simple linear considerations.

Key words: ISM: general – clouds – kinematics and dynamics – turbulence – stars: formation

1 INTRODUCTION

The effect of magnetic fields on the evolution of molecular clouds (MCs) is not yet fully understood, in particular concerning its effect on the formation of the clouds and their subsequent star formation processes(see, e.g., Passot et al. 1995; Hennebelle & Pérault 2000; Hartmann, Ballesteros-Paredes, & Bergin 2001; Ostriker et al. 2001; Kim et al. 2003; Inoue & Inutsuka 2008, 2009, 2012; Heitsch et al. 2009; Banerjee et al. 2009; Vázquez-Semadeni et al. 2011; Inutsuka et al. 2015; Körtgen & Banerjee 2015).

One scenario that has been recently proposed for the formation of MCs (in solar neighborhood-like conditions) is that of *colliding flows*, in which moderately supersonic streams of warm neutral medium (WNM) collide to produce a cold neutral cloud through nonlinear triggering of the thermal instability (TI; Hennebelle & Pérault 1999). The cloud becomes turbulent through the combined action of TI and various other dynamical instabilities, such as the nonlinear thin shell (NTSI), Kelvin-Helmholtz, and Rayleigh-Taylor instabilities (see, e.g., Vishniac 1994; Koyama & Inutsuka 2002; Heitsch et al. 2006; Vázquez-Semadeni et al. 2006). Moreover, as a cloud forms and grows out of compression in the WNM, it should become molecular, supercritical, and gravitationally unstable at roughly the same time (see e.g., Hartmann, Ballesteros-Paredes, & Bergin 2001), transiting to a regime of gravitational collapse. Because this mechanism can coherently produce large amounts of cold, dense gas, the newly formed clouds may contain numerous Jeans masses, and thus the collapse can proceed in a hierarchical fashion, roughly as predicted

* E-mail: manuelaz@umich.edu

© 2015 RAS

by Hoyle (1953), but aided by the fact that the cloud's internal turbulence produces nonlinear density fluctuations that have shorter free-fall times than the cloud at large (Heitsch & Hartmann 2008; Vázquez-Semadeni et al. 2009; Gómez & Vázquez-Semadeni 2014; Vázquez-Semadeni 2015). This mechanism provides a self-consistent way to generate the observed structure and dynamics of MCs and to regulate the evolution of the star formation rate (SFR) (e.g., Zamora-Avilés et al. 2012; Zamora-Avilés & Vázquez-Semadeni 2014).

However, as the magnetic field is ubiquitous in the Galaxy, it is expected to play a central role in the formation of clouds. The strength and orientation of the mean magnetic field with respect to the flows play a crucial role for the flow-driven formation of MCs, in particular for whether the clouds can become dense, massive and supercritical (e.g., Elmegreen 1994; Passot et al. 1995; Hennebelle & Pérault 2000; Hartmann, Ballesteros-Paredes, & Bergin 2001; Inoue & Inutsuka 2008, 2009, 2012; Heitsch et al. 2009; Banerjee et al. 2009; Vázquez-Semadeni et al. 2011; Heitsch & Hartmann 2014; Lazarian 2014; Körtgen & Banerjee 2015), simply because the gas can flow freely along field lines, but in the perpendicular direction it is opposed by the magnetic pressure, and because coherent compressions are sometimes deemed difficult to maintain over the required scales of hundreds of parsecs. Moreover, the magnetic tension tends to weaken or even suppress the dynamical instabilities (and thus the generation of turbulence) in the clouds assembled by colliding flows, particularly the NTSI (Heitsch et al. 2007, 2009) by preventing the transport of transverse momentum.

In this contribution, we extend the previous works on the formation of dense clouds in the presence of magnetic fields to consider the effects of the suppression of the instabilities on the star-forming activity of the clouds. To this effect, we consider the formation of magnetically supercritical clouds by colliding flows in the presence of self-gravity and a background field of different magnitudes, including a non-magnetic case. The plan of the paper is as follows: In Section 2 we describe the numerical model. The results are presented in Sec. 3 and discussed in Sec. 4. Finally, a summary and some conclusions are presented in Section 5.

2 NUMERICAL MODEL

2.1 Numerical scheme

We use the Eulerian adaptive mesh refinement (AMR) FLASH2.5 code (Fryxell et al. 2000) to perform three-dimensional, self gravitating, MHD simulations, including heating and cooling processes. We use an ideal MHD treatment since the diffusive processes such as ambipolar diffusion (AD) at the simulated scales are of the order of numerical noise, and their effect on the results are negligible, and comparable to those of numerical diffusion (Vázquez-Semadeni et al. 2011). The ideal MHD equations are solved using the MHD HLL3R solver, which preserves positive states for density and internal energy (Bouchut et al. 2002, 2010; Waagan 2009; Waagan et al. 2011). This solver is suitable for highly supersonic astrophysical problems, such as those studied here.

2.2 Heating and Cooling

We calculate the heating and cooling rates using the analytic fits by Koyama & Inutsuka (2002) for the heating ($\Gamma_{\rm KI}$) and cooling ($\Lambda_{\rm KI}$) functions (see also Vázquez-Semadeni et al. 2007, for corrections to typographical errors),

$$\Gamma_{\rm KI} = 2.0 \times 10^{-26}\,{\rm erg\,s^{-1}}, \tag{1}$$

$$\frac{\Lambda_{\rm KI}(T)}{\Gamma_{\rm KI}} = 10^7 \exp\left(\frac{-1.184\times10^5}{T+1000}\right) + \\ + 1.4\times10^{-2}\sqrt{T}\exp\left(\frac{-92}{T}\right)\ {\rm cm^3}, \tag{2}$$

which are based on the thermal and chemical calculations considered by Wolfire et al. (1995) and Koyama & Inutsuka (2000).

In the present study, we have chosen *not* to include any form of stellar feedback, in order to isolate the effects of varying the magnetic field. A study including stellar feedback will be presented elsewhere.

2.3 Refinement criterion and sink particles

In order to follow the development of high density regions, we employ a refinement criterion which, however, is not standard. The most frequently used criterion for refinement is the so-called Jeans criterion (Truelove et al. 1997), which aims to prevent artificial fragmentation, requiring that the local Jeans length be resolved by at least a certain minimum of grid cells. Because, at constant temperature, the Jeans length scales as $\rho^{-1/2}$, the condition of a fixed number of cells per Jeans length implies that the grid size also scales with density as $\Delta x \propto \rho^{-1/2}$. Instead, we have used a *constant mass* criterion, in which the grid size scales with density as $\Delta x \propto \rho^{-1/3}$, and so the mass of the new level of refined cells is the same as that of the previous level when it was created.[1] In section 4.2 we show that the effect in using the *constant mass* (in run B3) instead of the Jeans criterion (run B3J) is just a delay in the onset of star formation by $\sim 10\%$. Therefore, we do not consider that the usage of this criterion has any important consequences, since we are not concerned with the mass distribution of the sinks (related to the fragmentation), but only with the net SFR.

Once the maximum refinement level is reached in a given cell, a sink particle can be formed when the density in this cell exceeds a threshold number density, $\rho_{\rm thr} = 8.9\times10^{-18}\,{\rm g\ cm^{-3}}$ ($= 4.2\times10^6\,{\rm cm^{-3}}$), among other sink-formation tests (for a detailed description and the implementation in the FLASH code, see Federrath et al. 2010).

[1] The reason for this is that the present simulations are part of a larger set (to be presented elsewhere) that contains also simulations with stellar feedback, where the feedback is a function of the sink particle mass. In those simulations, the priority is for the feedback to be independent of resolution, and such a refinement criterion achieves this goal.

Table 1. List of simulations

Run name	$\lvert B_{x,0}\rvert$ (μG)	$\mu/\mu_{\rm crit}$ [a]	Refinement criterion[b]
B0	0	∞	constant mass
B1	1	4.76	constant mass
B2	2	2.38	constant mass
B3	3	1.59	constant mass
B3J	3	1.59	Jeans

[a] We adopt $\mu_{\rm crit} = 0.16/\sqrt{(}G)$, appropriate value for sheet-like clouds (Nakano & Nakamura 1978). Note that all models are magnetically supercritical.
[b] See Section 4.2 for a discussion about the refinement criteria.

The sink is formed with the excess mass within the cell, that is, $M_{\rm Sink} = (\rho - \rho_{\rm thr})\Delta x^3$. The sink particles can then accrete mass (with $\rho > \rho_{\rm thr}$) from their surroundings (within an accretion radius of $\sim 2.5\Delta x$) (Federrath et al. 2010).

2.4 Initial conditions

We use a setup similar to that of Vázquez-Semadeni et al. (2007). The numerical periodic box, of dimensions $L_x = 256\,$pc and $L_y = L_z = 128\,$pc, is initially filled with warm neutral gas at a uniform density $n = 2\,{\rm cm}^{-3}$ and constant temperature of 1450 K, which corresponds to thermal equilibrium and implies an adiabatic sound speed of $4.0\,{\rm km\ s}^{-1}$. Assuming a composition of atomic hydrogen only (with a mean molecular weight $\mu = 1.27$), the gas mass in the whole box is $\sim 2.6 \times 10^5\,M_\odot$, whereas the mass contained in the cylinders is $\sim 4.5 \times 10^4\,M_\odot$.

The initial velocity field contains a random component in magnitude and direction, with a maximum amplitude of $2.1\,{\rm km\ s}^{-1}$. On top of this random field, we add two cylindrical streams, each of radius $R_{\rm inf} = 32\,$pc and length $L_{\rm inf} = 112\,$pc, moving in opposite directions at a moderately supersonic velocity of $7.5\,{\rm km\ s}^{-1}$ in the x-direction (implying a Mach number $\mathcal{M}_{\rm inf} \simeq 1.89$ with respect to the adiabatic sound speed in the WNM).

The numerical box is permeated with a uniform magnetic field along the x-direction, for which we consider three different strengths (1, 2, and $3\,\mu$G), along with a nonmagnetic case. Note that the corresponding mass-to-flux ratios are greater than the critical value, so that our clouds are magnetically supercritical in all cases, in agreement with observations that suggest that MCs are in general magnetically supercritical (Crutcher et al. 2010). Table 1 gives a summary of the magnetic parameters of the simulations. Finally, the maximum resolution reached is $\Delta x = 0.03\,$pc.

With this setup and initial conditions we perform four (otherwise identical) simulations, varying only the magnetic field strength. We only consider the case where the magnetic field is initially aligned with the inflows (along the x direction), but note that non-aligned cases can lead to motions along the magnetic field for sufficiently high inflow speeds at a given field strength (see, e.g., Hennebelle & Pérault 2000; Körtgen & Banerjee 2015).

3 RESULTS

Henceforth, the analysis focuses on the "central box" of the simulation, a cylindrical region of radius 40 pc and length of 80 pc, centered at the plane where the flows collide. We will refer to the cold cloud formed in this box as the "central cloud", or simply, "the cloud", and here we will consider its global physical properties.

3.1 Global evolution

The collision of WNM streams (or *inflows*) in the center of the numerical box nonlinearly triggers thermal instability (TI), forming a thin cloud of cold atomic gas (see, e.g., Hennebelle & Pérault 1999; Koyama & Inutsuka 2000, 2002; Walder & Folini 2000), which at the same time becomes turbulent by the combined action of TI with various other dynamical instabilities (see, e.g., Hunter et al. 1986; Vishniac 1994; Koyama & Inutsuka 2002; Heitsch et al. 2005; Vázquez-Semadeni et al. 2006). Also, the total (thermal plus ram) pressure in the dense gas is in balance with the total pressure of the surrounding WNM, while the thermal pressures are also equal because of the rapid condensation caused by TI. It was shown by Banerjee et al. (2009) that the two conditions combined imply similar turbulent Mach numbers in both the diffuse and the dense gas, and so the cold, dense gas exhibits a moderately supersonic velocity dispersion. Since we do not follow the chemistry we indistinctly will refer to the dense gas ($n > 100\,{\rm cm}^{-3}$) as "molecular".

Since our numerical boxes are magnetically supercritical (see Table 1), the clouds soon become dominated by self-gravity[2] and begin to contract gravitationally as a whole. During the large-scale contraction, the local, nonlinear (i.e., large-amplitude) density enhancements produced by the initial turbulence manage to complete a collapse of their own, since their local free-fall time is shorter than the average one for the entire cloud (Vázquez-Semadeni et al. 2007, 2009; Heitsch & Hartmann 2008; Pon et al. 2011). These local collapses involve only a small fraction of the cloud's total mass (see Sec. 3.5).

3.2 Cloud structure

Figures 1 and 2 illustrate the morphological effects of magnetic fields at $t = 5$, 10, 15, 19, and 25 Myr. In Fig. 1 we show $t = 19$ Myr rather than 20 Myr in order to show all four simulations, since run B2 terminates before this time.

In these figures, the various columns from left to right represent column density maps of the "central clouds" for models B0, B1, B2, and B3 ($B_{x,0} = 0$, 1, 2, and $3\,\mu$G, respectively) in face-on and edge-on views. The morphologies (in column density maps) are consistent with those reported

[2] As Hartmann, Ballesteros-Paredes, & Bergin (2001); Vázquez-Semadeni et al. (2011); Heitsch & Hartmann (2014) pointed out, MCs start in a magnetically subcritical state, but they eventually become supercritical itself simply by mass accretion along the magnetic field lines.

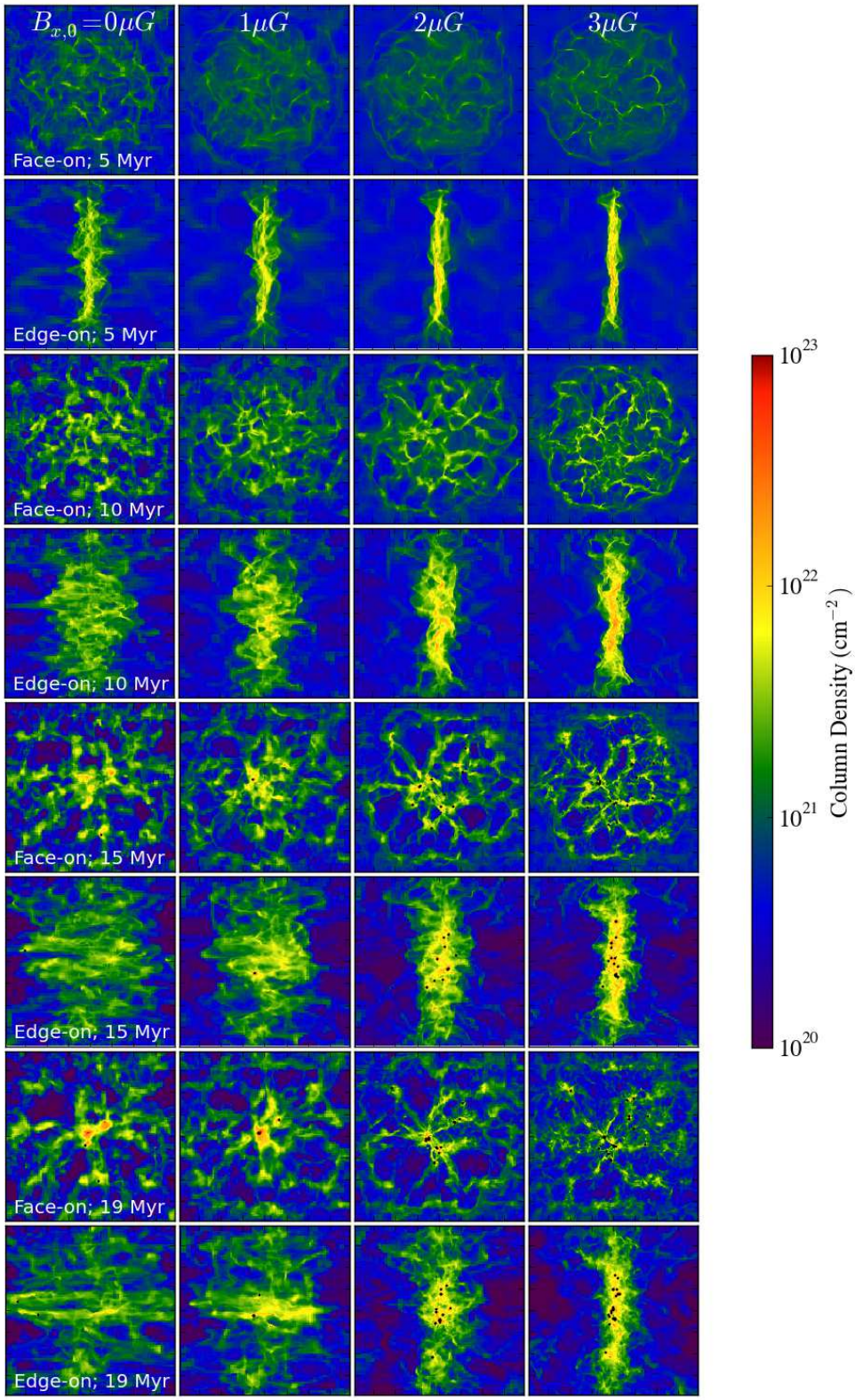

Figure 1. Face-on and edge-on column density views of the "central clouds" at $t = 5$, 10, 15, and 19 Myr. The different columns represent the models B0 ($B_{x,0} = 0\,\mu$G), B1 (1 μG), B2 (2 μG), and B3 (3 μG). The dots (in panels at $t = 15$ and 19 Myr) represent the projected position of the sink particles, i.e., collapsed objects. The box is 80 pc per side. Note that in the simulations with larger magnetic field strengths, the clouds are more coherent and compact.

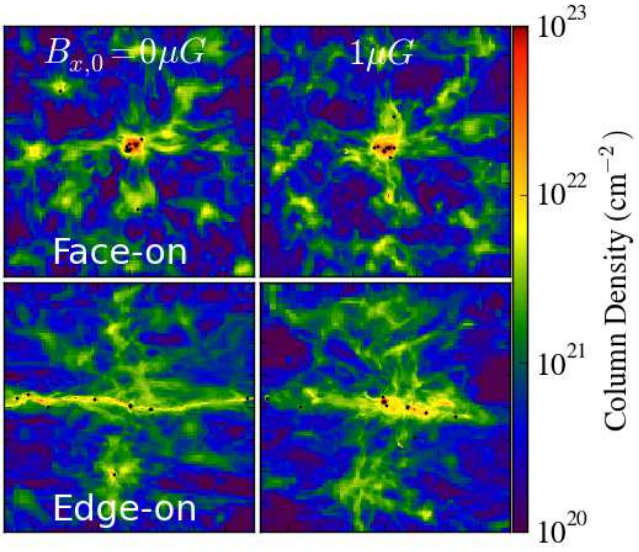

Figure 2. Same as Fig. 1, but at $t = 25$ Myr. By this time, runs B2 and B3 have already been terminated.

by Heitsch et al. (2009, see their models H, X25, and X50 in their Figure 1).

From these figures, it is seen that *increasing the magnetic field strength prevents the cloud from reexpanding in the direction of the inflows, as well as from growing in the direction perpendicular to them* after they collide. This can be interpreted as an inhibition of the NTSI by the magnetic field (see also, Heitsch et al. 2007, 2009). We speculate that this occurs because the magnetic field, which is parallel to the inflows, inhibits the transverse motions that would develop as a consequence of the NTSI,[3] and therefore allows for more efficient dissipation of the inflow kinetic energy by forcing a more focused collision of the two streams.

To test for this speculation, in the *left panel* of Fig. 3 we show the evolution of the velocity dispersion in the plane perpendicular to the inflows. It is seen that this transverse component is significantly suppressed during the early stages ($t \lesssim 5$ Myr) in the magnetic cases, especially in runs B2 and B3. As a consequence, the re-expansion motion of the compressed layer is inhibited, as illustrated in the *right panel* of Fig. 3, which shows the longitudinal (parallel to the inflows) velocity dispersion of the dense ($n > 100\mathrm{cm}^{-3}$) gas. We consider the dense gas only in order to avoid including the longitudinal motion of the inflows. This longitudinal velocity dispersion is seen to be strongly suppressed during the early stages (again, $t \lesssim 5$ Myr) as the field strength is increased, by up to a factor of $\sim 4\times$ between the non-magnetic simulation B0 and that with $B = 3\,\mu$G (B3).

This mechanism leads to the formation of clouds that, in the more strongly magnetized cases (runs B2 and B3), are denser on average, although, somewhat unexpectedly, at early times they contain a highly more complex filamentary structure, which is characterized by sharper, thinner filaments embedded in a diffuse background (models B2 and B3), while models B0 and B1 are characterized by more roundish structures and less contrast with the background.

This suggests that the stronger NTSI, and therefore stronger turbulence in the less magnetized cases tends to disrupt the filaments that are produced by the thermal instability (TI; e.g., Vázquez-Semadeni et al. 2000; Audit & Hennebelle 2005; Vázquez-Semadeni et al. 2006). Indeed, this can be seen in the density probability density function (density PDF) of the simulations, shown in Fig. 4. In this figure, it can be seen that the more strongly magnetized runs (B2 and B3) tend to have a deficit of gas in the range $10\,\mathrm{cm}^{-3} \lesssim n \lesssim 10^2\mathrm{cm}^{-3}$ and an excess of gas at densities $10^2\mathrm{cm}^{-3} \lesssim n \lesssim 10^3\mathrm{cm}^{-3}$, especially at times $t = 5$ and 10 Myr, where the dynamics is still not strongly dominated by gravity, but rather by the interaction between turbulence and TI. This suggests that the filaments have densities $n \sim 10^2$–$10^3\,\mathrm{cm}^{-3}$, and are more abundant at stronger magnetic field strengths, while instead they tend to be destroyed by turbulence at weaker field strengths.

3.3 Evolution of the Density PDFs

The different evolution of the clouds caused by the difference in the background magnetic field is also reflected on their volume-weighted density PDFs (see Fig. 4). Although in general the PDFs of all four runs exhibit the bimodal shape characteristic of thermally bistable flows (e.g., Vázquez-Semadeni et al. 2000; Audit & Hennebelle 2005; Gazol et al. 2005), with maxima at $n \sim 0.3\,\mathrm{cm}^{-3}$ and $30\,\mathrm{cm}^{-3}$, these features do not develop clearly until $t \sim 10$ Myr. At earlier times ($t \sim 5$ Myr), as mentioned in Sec. 3.2, a prominent feature corresponding to the early filament formation is present at $n \sim 100\,\mathrm{cm}^{-3}$, although it is more pronounced in cases with stronger magnetic fields, indicating that the stronger level of turbulence generated in the cases with weaker fields partially disrupts the filaments, or prevents their formation.

At later times, the increasing dominance of gravity leaves its imprint on the PDFs. Interestingly, at 15 Myr (see lower left panel of Fig. 4), the density PDF for all runs exhibits two power low tails at high densities, a feature recently reported in observations toward GMCs (see, e.g., Schneider et al. 2015). As time progresses, the dense gas fraction increases, the increase being faster in the more strongly magnetized cases (see this trend in the upper right and lower left panels of Fig. 4), an effect that is directly reflected in a faster increase of the SFR (see Section 3.5). However, at the time at which the star formation efficiency (SFE; eq. [3]) is 10% in each run (at $t = 25.0$, 19.8, 16.6, and

[3] Recall the NTSI acts by increasing the curvature of bending perturbations on the boundary of the dense compressed layer and pushing the gas towards the nodes of these perturbations. The gas therefore moves in a direction oblique to the inflows, effectively transferring part of the momentum from the inflows to the direction perpendicular to them (Vishniac 1994). The oblique convergence of gas at opposite sides of the nodes finally results in a compression and acceleration of the gas in the nodes parallel to the inflows, but moving in the opposite direction, which ultimately produces an expansion of the layer (e.g., Folini & Walder 2006).

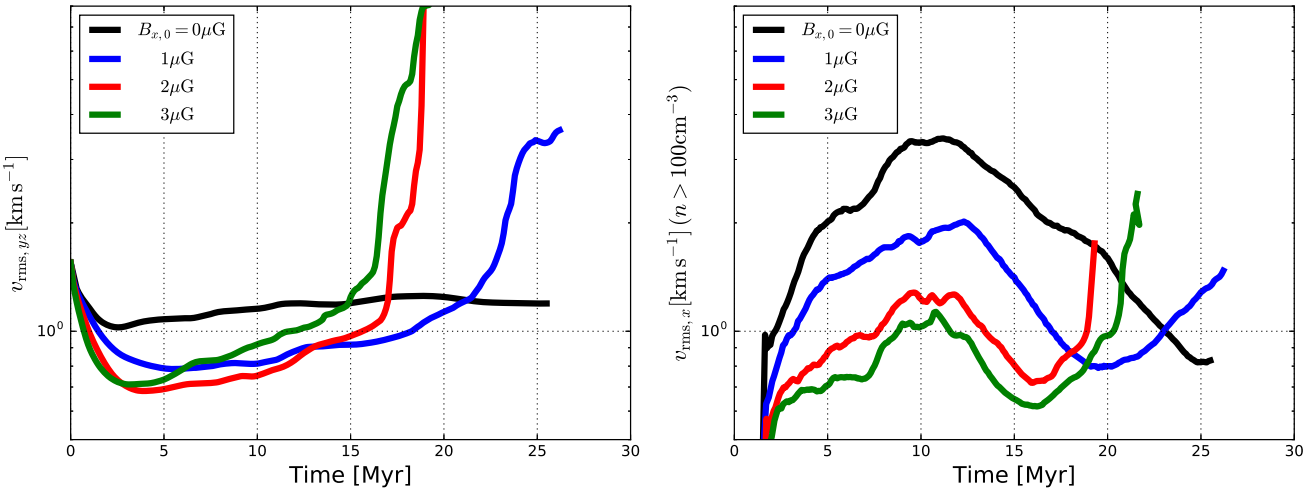

Figure 3. *Left:* Evolution of the transverse velocity dispersion (in the plane perpendicular to the inflows) for all the gas in the "central box" (a cylinder of length and diameter equal to 80 pc, centered at the plane where the inflows collide; see Sec. 3) for the 4 simulations. It is seen that this dispersion decreases for progressively larger magnetic field strength, being almost 4 times larger in the non-magnetic case than in the case with $B = 3\,\mu$G. The strong increase of the transverse velocity dispersion in the magnetic runs B1, B2 and B3 toward the final stages of the simulations is due to the gravitational contraction. *Right:* Evolution of the longitudinal velocity dispersion in the same box, considering only the dense gas ($n > 100{\rm cm^{-3}}$) in order to avoid picking up the inflows.

15.5 Myr for the models B0, B1, B2 and B3, respectively), the trend is reversed because at weaker field strengths the collapse takes longer to initiate, since the cloud was initially more dispersed. Nevertheless, at later times the collapse does proceed more freely for weaker field strength. This is reflected in the fact that run B0 takes 10 Myr more than run B3 to reach an SFE of 10%, but by the time it does so, its star formation rate (SFR) is increasing faster (cf. Sec. 3.5).

Finally, note that, in all runs, we terminate the inflows at $t \sim 15$ Myr, and therefore the clouds are no longer fed by the diffuse gas inflows after this time. Thus, from this time on, the volume occupied by the dense gas ($n > 100\,{\rm cm^{-3}}$) decreases while its mean density increases (Fig. 5), which is a clear sign of global collapse, even for the more diffuse and less compact clouds (models B0 and B1).

3.4 Cloud mass

Figure 6 shows the effect of increasing the magnetic field strength on the cloud mass. It is seen that models with higher magnetic field strength produce more massive clouds, by up to a factor of 3 (compare, for instance, models B0 and B3). This result is in accordance with simulations with a similar setup by Heitsch et al. (2009) (see their Figure 2), but without self-gravity. This suggests that the stronger turbulence in the weakly magnetized cases counteracts the transition from the warm to the cold phase induced by TI, effectively reducing the amount of cold, dense gas produced.

3.5 The Star Formation Rate and Efficiency

The star formation activity in the simulations exhibits strong intermittency in both space and time. Because the clouds are contracting gravitationally, they are becoming denser on average. As shown by Zamora-Avilés et al. (2012), this implies that quantities such as the SFE and SFR are naturally time-dependent, and increase in time until feedback (not included in the present study) begins to destroy the clouds.

As in previous works (e.g., Vázquez-Semadeni et al. 2007, 2010; Zamora-Avilés et al. 2012; Colín et al. 2013; Zamora-Avilés & Vázquez-Semadeni 2014), we define the instantaneous SFE as

$$\mathrm{SFE}(t) = \frac{M_{\rm S}(t)}{M_{\rm C}(t) + M_{\rm S}(t)}, \qquad (3)$$

where $M_{\rm C}$ is the cloud mass (specifically, the gas mass at $n > 100\,{\rm cm^{-3}}$), and $M_{\rm S}$ is the total mass in stars, which we take as the total mass in sinks, $M_{\rm sinks}$.

We estimate the SFR as the time derivative of the total sink mass, $dM_{\rm sinks}(t)/dt$ (which is calculated by dividing the difference in the total sink mass in a time step by the duration of the step). This accounts for both the mass collapsed onto new sinks and the mass accreted onto the existing ones. Figures 7 and 8 show the time evolution of the SFR and SFE for the various simulations with different initial strengths of magnetic field. In general, it is seen that both the SFE and the SFR increase monotonically in time until the end of the simulations. This is due to the inherent increase of the SFR caused by the collapse of the clouds, and to the neglect of stellar feedback (cf. Sec. 2.2), which has been shown previously to partially or completely suppress the SF activity in the clouds, depending on their mass (and possibly geometry) (e.g., Vázquez-Semadeni et al. 2010; Dale et al. 2012, 2013; Colín et al. 2013). Therefore, in the present simulations, there is no agent that prevents the continued increase

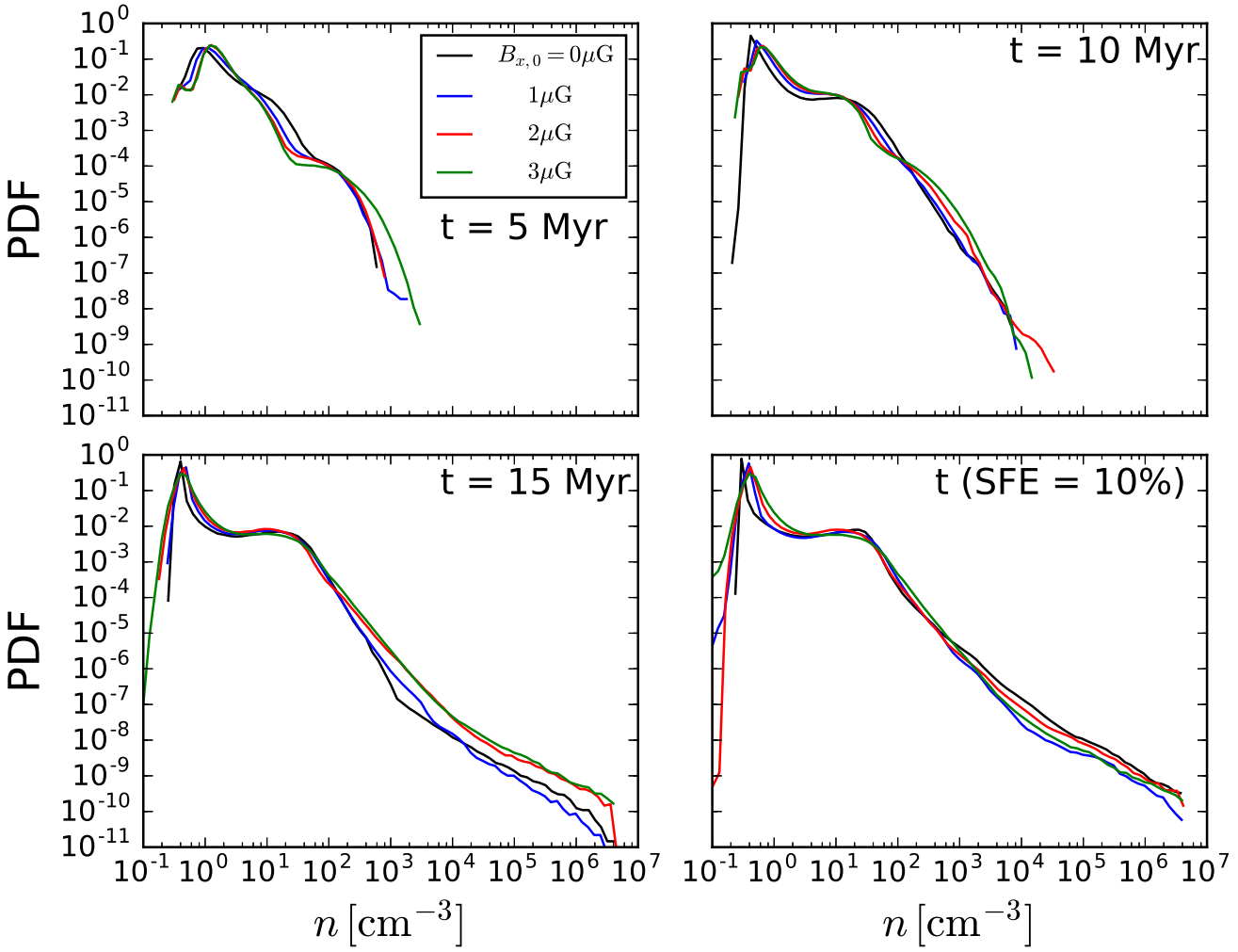

Figure 4. Volume-weighted density PDF for the different models at $t = 5$, 10, and 15 Myr for the central box (of 80 pc per side). The lower right panel shows the density PDFs for all the models at the time at which the star formation efficiency is 10% ($t = 25.0$, 19.8, 16.6, and 15.5 Myr, corresponding to models B0, B1, B2 and B3, respectively).

of the SFR. However, this allows us to investigate the effects of varying the magnetic field alone.

In this context, several points are worth noting in Figs. 7 and 8. First, it is seen that the onset of SF is delayed by larger amounts at weaker values of the magnetic field strength, although it is nearly simultaneous for runs B1 and B0. Morever, while run B2 and B3 start forming sinks *before* the inflows end ($t \sim 15$ Myr), runs B0 and B1 only begin forming sinks when the inflows have ended. Second, run B0 exhibits an initial period of nearly 2 Myr during which the SFR *decreases*, but after that time, its SFR begins increasing. A similar initial decrease of the SFR is observed in run B1, although its duration is shorter, ~ 1 Myr. Third, it is seen that, once the SFRs of all simulations are increasing, the SFR increase rate of run B0 is larger than that of the magnetic runs (see Section 3.3). Finally, note that the SFE (as well as the SFR) is much higher than that typically observed in GMCs ($\sim 2\%$, e.g., Myers et al. 1986) due to the absence of stellar feedback (see Secs. 2.2 and 4.3.1). However, this is not a problem because here we are not attempting to reproduce actual observed SFEs, but rather to isolate the effects of varying the magnetic field on the SFR and the SFE.

4 DISCUSSION

4.1 Comparison with previous work

The effect of the magnetic field strength and orientation in the assembly and star-forming activity of MCs has been addressed by several studies in the past (see, e.g., Passot et al. 1995; Hennebelle & Pérault 2000; Ballesteros-Paredes & Mac Low 2002; Heitsch et al. 2009; Banerjee et al. 2009; Vázquez-Semadeni et al. 2011; Hill et al. 2012; Walch et al. 2015b; Körtgen & Banerjee

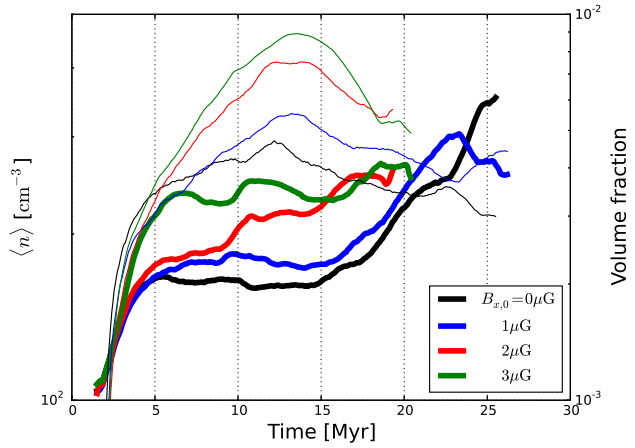

Figure 5. Evolution of the mean number density of dense gas ($n > 100\,\mathrm{cm}^{-3}$; thick lines) of the "central cloud" in the simulations with $B_{x,0} = 0$, 1, 2, and $3\,\mu$G. The thin lines represent the volume fraction of the dense gas in the central boxes.

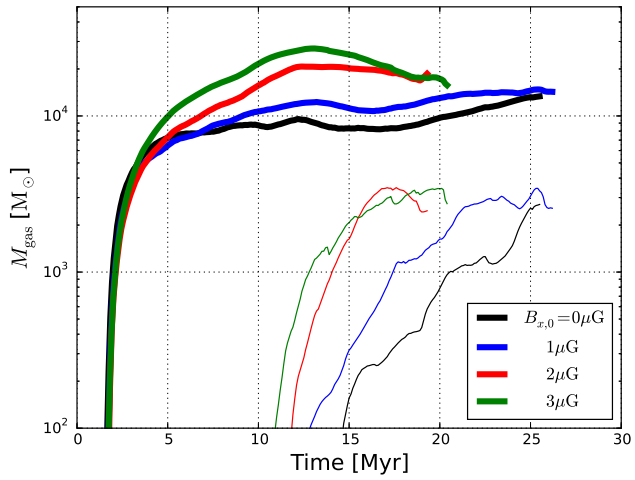

Figure 6. Evolution of the dense gas mass with $n > 100\,\mathrm{cm}^{-3}$ (thick lines) and $n > 10^4\,\mathrm{cm}^{-3}$ (thin lines) of the "central cloud" for the simulations with $B_{x,0} = 0$, 1, 2, and $3\,\mu$G. Simulations with higher (initial) magnetic field strength produce more massive clouds.

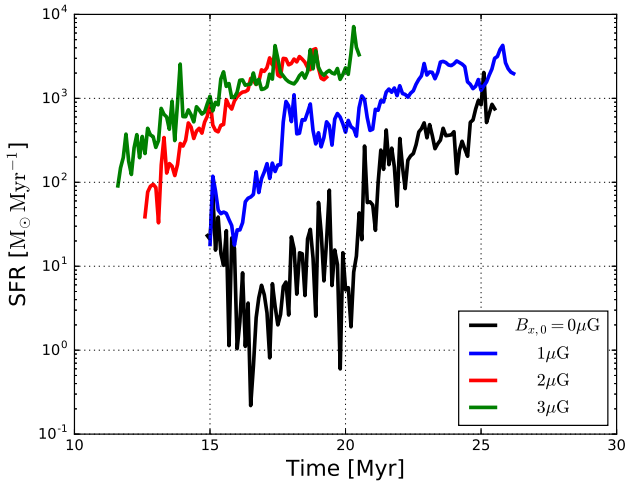

Figure 7. Evolution of the SFR. The onset of SF is seen to be delayed as the background magnetic field strength is decreased, although it is nearly simultaneous for runs B1 and B0.

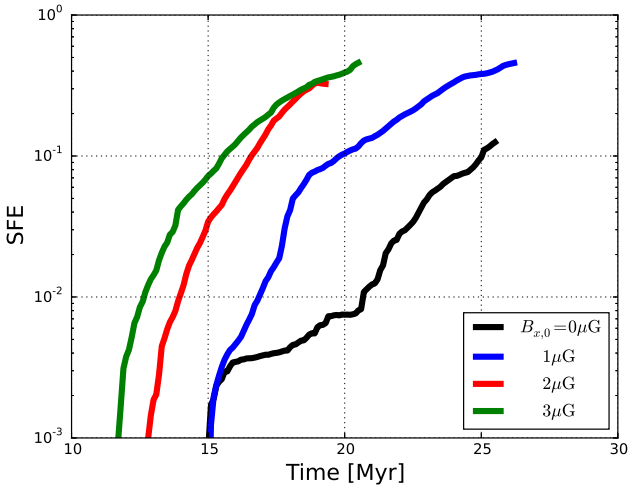

Figure 8. Evolution of the star formation efficiency (SFE; see eq. 3) for the four simulations. Note that, because stellar feedback is not included (cf. Sec. refsec:heating-cooling), the SFE is seen to reach values larger than observed values for whole GMCs.

2015). In particular, Passot et al. (1995) showed that the dependence of the SFR on the magnetic field strength is highly non-monotonic. In particular, at intermediate magnetic field strengths, an increase of the uniform background field tends to suppress shearing motions in the medium that disrupt clouds, thereby promoting the growth of density fluctuations (see also Ballesteros-Paredes & Mac Low 2002). In our case, the shearing motions are caused by the NTSI, and their inhibition by the magnetic field leads to the formation of more massive clouds (cf. Sec. 3.4 and Fig. 6) and therefore a larger total stellar mass (Fig, 9). The latter shows the total mass in sinks 5 Myr after the onset of star formation in all runs, and can be compared to Figure 8 in Passot et al. (1995). Note that although the setup of those authors was very different from ours (as well as the numerical techniques), and the shearing in the study of those authors was due to differential galactic rotation, not the NTSI, the effect of magnetic fields on reducing shearing motions that inhibit contraction is similar.

In addition, our results are consistent with those of Heitsch et al. (2009), who also studied the problem of cloud formation by converging flows in the case where the magnetic fields are aligned with the flows, although they considered only the role of the magnetic field in the process of cloud formation, excluding self-gravity (see also Heitsch et al. 2007). Those authors found that increasing the magnetic field strength tends to weaken (or even suppress) the NTSI, which results in clouds with reduced levels

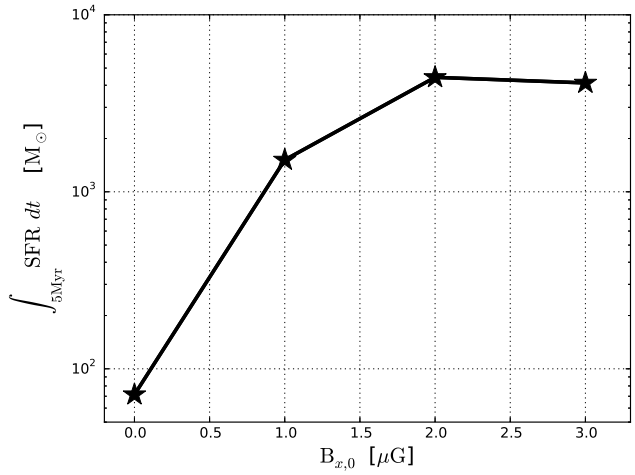

Figure 9. Total mass in sinks 5 Myr after the onset of star formation (i.e., the SFR integrated during this time interval) for all runs. Note that, on average, the star formation activity increases with increasing magnetic field strength.

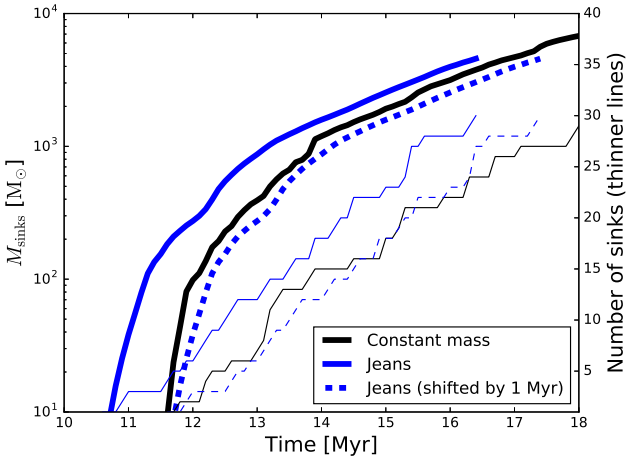

Figure 10. Time evolution of the number and the total mass in sinks for runs B3 (which uses the *constant mass* refinement criterion) and B3J (Jeans criterion). Note that both, the number and the total mass in sinks are very similar when we consider the curves for the run B3J shifted by 1 Myr.

of turbulence, larger masses and smaller sizes, in agreement with our results (see Fig. 6).

Our findings can also be compared to those of Carroll-Nellenback et al. (2014, hereafter CN+14), who used a setup similar to ours, but not including the magnetic field. Interestingly, rather than investigating the effect of variations of the intensity of the background magnetic field, those authors were concerned with the effect of pre-existing clumpiness in the colliding flows. They found that clouds formed by clumpy inflows are in general more turbulent and have lower total mass (gas + sinks) as well as fewer but more massive sink particles. Therefore, the cloud formed by clumpy inflows in that study is similar to the clouds formed at lower field strengths in our case, although for a different reason: in the case of CN+14, the cloud is scattered because the clumpiness of the incoming flows reduces the amount of mass that collides directly against material from the opposing inflow, thus reducing the dissipation of the kinetic energy of the inflows. Instead, in our case, the presence of progressively stronger magnetic fields causes a suppression of the NTSI, reducing the generation of turbulence in the cloud, as well as the "bounce" that results from the development of the instability (see Sec. 3.2).

4.2 Test of the refinement criterion

Our *constant-mass* refinement criterion does not fulfill the Truelove criterion (Truelove et al. 1997) for prevention of spurious fragmentation. This criterion requires the resolution to scale linearly with the Jeans length L_{J} (i.e., as $\rho^{-1/2}$, assuming constant temperature). Instead, with our criterion, the resolution scales as $\rho^{-1/3}$, or equivalently, as $L_{\mathrm{J}}^{2/3}$, implying that the Jeans length is increasingly more poorly resolved as the density increases, and therefore, some artificial fragmentation is expected.

In order to quantify this effect, we performed an additional simulation, labeled B3J, which is identical to run B3 except for the refinement criterion used. For run B3J we use the Jeans criterion and we resolve the Jeans length by 10 grid cells in order to fulfill the Truelove criterion.[4] Figure 10 shows the evolution of the number of sink particles and the total mass in them. It can be seen that both quantities are very close for the two simulations, and that the effect of choosing the Jeans criterion over the *constant mass* criterion is just to delay the onset of star formation by 10%. Therefore, the effect of the refinement criterion on our results is negligible compared to the offsets in the SFR caused by the magnetic field, as discussed in Sec. 3.5.

4.3 Limitations

4.3.1 Neglected processes

One of the most notable omissions in our simulations is that of stellar feedback. In particular, the ionizing radiation from massive stars is generally considered to be the dominant mechanism of stellar energy injection into GMCs (Matzner 2002), although its effect may be mostly the dispersal of the clouds rather than maintaining them in a near-equilibrium state and reducing both the SFR and the SFE (Vázquez-Semadeni et al. 2010; Zamora-Avilés et al. 2012; Dale et al. 2012, 2013; Colín et al. 2013). Moreover, after a few Myr, SN explosions are expected to begin occurring, contributing to further cloud dispersal, although the effect may not be stronger than that of ionizing radiation (e.g., Walch & Naab 2015a; Iffrig & Hennebelle 2015; Körtgen et al. 2016).

Nevertheless, as mentioned above, in this paper we have not been concerned so much about generating a realistic

[4] The corresponding threshold density for sink formation is $\rho_{\mathrm{thr}} = 7.1 \times 10^{-20}$ g cm^{-3}(= 1.8×10^4 cm^{-3}).

model of MCs at all times in their evolution, but rather in performing a series of numerical experiments assessing the effect of the uniform magnetic field strength in setting up the initial conditions of the clouds. For this purpose, our numerical simulations are appropriate.

5 SUMMARY AND CONCLUSIONS

In this paper, we have presented four MHD simulations aimed at studying the evolution of MCs formed by diffuse converging flows in the presence of magnetic fields, in order to investigate the effect of the latter on the development of the initial conditions of the nascent clouds and their early star formation activity. We have considered four otherwise identical numerical models except for the initial magnetic field strength, for which we have considered the values 0, 1, 2, and 3 μG (models B0, B1, B2, and B3, respectively), corresponding to magnetically supercritical configurations in all cases. The field is initially aligned with the flows. The latter is not a restrictive condition, however, since it has been shown that, when the flows are oblique to the magnetic field and have sufficiently high Mach numbers (depending on the field strength), the flows are reoriented to proceed along the magnetic field (Hennebelle & Pérault 2000). Therefore, whenever the flows manage to collide, they will do so aligned with the field.

In the initial phase of cloud formation, our simulations show that, in agreement with the non-self-gravitating results from Heitsch et al. (2009), the presence of a magnetic field aligned with the inflows tends to suppress the NTSI, causing the clouds to be more compact, denser, and less turbulent. In the presence of self-gravity, this leads to an earlier global collapse of the clouds, and to an enhanced early star-formation activity. Instead, more weakly magnetized, or fully non-magnetic cases produce more dispersed and more turbulent clouds, that initially expand in a rebound from the initial collision, and only later begin to collapse. However, when they do so, their SFRs increase more rapidly, because the collapse is then unimpeded by the magnetic field.

Moreover, the non-magnetic simulation, run B0, and that with the weakest magnetic field (B1), do not start their collapse until the inflows are terminated.[5] Nevertheless, because the accepted value of the mean magnetic field strength in the ISM is comparable to that considered in our more strongly magnetized cases (runs B2 and B3; Crutcher et al. 2010), our results reinforce the notion that the turbulence produced by the stream collision in the nascent clouds is not enough to support them against their self-gravity (Vázquez-Semadeni et al. 2007), and therefore engage in global gravitational contraction soon after they are assembled.

This conclusion is further reinforced by the fact that the clouds in runs B0 and B1, which *are* supported by turbulence in their initial stages, do not begin forming stars until *after* the inflows, and therefore the turbulence driving, are terminated, and the clouds engage in global gravitational contraction. This suggests that *star-forming* GMCs are in general in a state of global collapse.

[5] Note that this does not necessarily imply that the turbulence generated by the inflows is sufficient to support the clouds, since it is possible that, had the inflows be maintained for longer times, the clouds might have gathered enough mass as to begin their collapse. Further study is necessary in order to address this issue.

ACKNOWLEDGEMENTS

We thankfully acknowledge Fabian Heitsch for stimulating discussions. MZA acknowledges hospitality offered by Robi Banerjee and Ralf Klessen at Hamburg Observatory (University of Hamburg) and Institute of Theoretical Astrophysics (University of Heidelberg) during the first stages of this work, and financial support from PAPIIT grants IN111313 and IN110214, CONACyT grant CB152913, and CONACyT postdoctoral fellowship at University of Michigan. RB and BK acknowledge funding from the German Science Foundation (DFG) for this project via the ISM-SPP 1573 grant BA 3706/3-1 and BA 3706/3-2. RB also acknowledge funding from the DFG via the grant BA 3706/4-1. LH was supported in part by NASA grant NNX16AB46G and by the University of Michigan. We also acknowledge Gilberto Zavala Pérez, Alfonso H. Ginori González, and Miguel Espejel Cruz for their valuable computational support. The numerical simulations presented here were performed on the *Calzonzin* cluster at Instituto de Radioastronomía y Astrofísica (Universidad Nacional Autónoma México), acquired through the CONACYT grant 102488 to EVS. The visualisation was carried out with the yt software (Turk et al. 2011). The FLASH code used in this work was in part developed by the DOE NNSA-ASC OASCR Flash Center at the University of Chicago.This research has made use of NASA's Astrophysics Data System Abstract Service.

REFERENCES

André, P., Di Francesco, J., Ward-Thompson, D., et al. 2014, Protostars and Planets VI, 27
Audit, E., & Hennebelle, P. 2005, A& A, 433, 1
Ballesteros-Paredes, J., & Mac Low, M.-M. 2002, ApJ, 570, 734
Ballesteros-Paredes,J., Vázquez-Semadeni, E., Gazol, A., et al. 2011b, MNRAS, 416, 1436
Banerjee, R., Vázquez-Semadeni, E., Hennebelle, P., & Klessen, R. S. 2009, MNRAS, 398, 1082
Bouchut F., Klingenberg C., Waagan K., 2007, Numer. Mathe., 108, 7
Bouchut F., Klingenberg C., Waagan K., 2010, Numer. Math., 115, 647
Carroll-Nellenback, J. J., Frank, A., & Heitsch, F. 2014, ApJ, 790, 37
Colín, P., Vázquez-Semadeni, E., & Gómez, G. C. 2013, MNRAS, 435, 1701
Crutcher, R. M., Wandelt, B., Heiles, C., Falgarone, E., & Troland, T. H. 2010, ApJ, 725, 466

Dale, J. E., Ercolano, B., & Bonnell, I. A. 2012, MNRAS, 424, 377
Dale, J. E., Ngoumou, J., Ercolano, B., & Bonnell, I. A. 2013, MNRAS, 436, 3430
Elmegreen, B. G. 1994, ApJ, 433, 39
Federrath, C., Banerjee, R., Clark, P. C., & Klessen, R. S. 2010, ApJ, 713, 269
Folini, D., & Walder, R. 2006, A& A, 459, 1
Fryxell, B., Olson, K., Ricker, P., et al. 2000, ApJS, 131, 273
Gazol, A., Vázquez-Semadeni, E., & Kim, J. 2005, ApJ, 630, 911
Gómez, G. C., & Vázquez-Semadeni, E. 2014, ApJ, 791, 124
Hartmann, L., Ballesteros-Paredes, J., & Bergin, E. A. 2001, ApJ, 562, 852
Heitsch, F., Burkert, A., Hartmann, L. W., Slyz, A. D., & Devriendt, J. E. G. 2005, ApJL, 633, L113
Heitsch, F., & Hartmann, L. 2008, ApJ, 689, 290
Heitsch, F., & Hartmann, L. 2014, MNRAS, 443, 230
Heitsch, F., Slyz, A. D., Devriendt, J. E. G., Hartmann, L. W., & Burkert, A. 2006, ApJ, 648, 1052
Heitsch, F., Slyz, A. D., Devriendt, J. E. G., Hartmann, L. W., & Burkert, A. 2007, ApJ, 665, 445
Heitsch, F., Stone, J. M., & Hartmann, L. W. 2009, ApJ, 695, 248
Hennebelle, P., & Pérault, M. 1999, A& A, 351, 309
Hennebelle, P., & Pérault, M. 2000, A& A, 359, 1124
Hill, A. S., Joung, M. R., Mac Low, M.-M., et al. 2012, ApJ, 750, 104
Hunter, J. H., Jr., Sandford, M. T., II, Whitaker, R. W., & Klein, R. I. 1986, ApJ, 305, 309
Hoyle, F. 1953, ApJ, 118, 513
Kim, W.-T., & Ostriker, E. C. 2002, ApJ, 570, 132
Iffrig, O., & Hennebelle, P. 2015, A& A, 576, A95
Inoue, T., & Inutsuka, S.-i. 2008, ApJ, 687, 303-310
Inoue, T., & Inutsuka, S.-i. 2009, ApJ, 704, 161
Inoue, T., & Inutsuka, S.-i. 2012, ApJ, 759, 35
Inutsuka, S.-i., Inoue, T., Iwasaki, K., & Hosokawa, T. 2015, A& A, 580, A49
Kim, W.-T., Ostriker, E. C., & Stone, J. M. 2003, ApJ, 599, 1157
Körtgen, B., & Banerjee, R. 2015, MNRAS, 451, 3340
Körtgen, B., Seifried, D., Banerjee, R., Vázquez-Semadeni, E., & Zamora-Avilés, M. 2016, MNRAS,
Koyama, H., & Inutsuka, S.-I. 2000, ApJ, 532, 980
Koyama, H., & Inutsuka, S.-i. 2002, ApJL, 564, L97
Lazarian, A. 2014, SSRv, 181, 1
Matzner, C. D. 2002, ApJ, 566, 302
Myers, P. C., Dame, T. M., Thaddeus, P., et al. 1986, ApJ, 301, 398
Nakano, T., & Nakamura, T. 1978, PASJ, 30, 671
Ostriker, E. C., Stone, J. M., & Gammie, C. F. 2001, ApJ, 546, 980
Passot, T., Vazquez-Semadeni, E., & Pouquet, A. 1995, ApJ, 455, 536
Pon, A., Johnstone, D., & Heitsch, F. 2011, ApJ, 740, 88
Schneider, N., Bontemps, S., Girichidis, P., et al. 2015, MNRAS, 453, 41
Smith, R. J., Glover, S. C. O., & Klessen, R. S. 2014, MNRAS, 445, 2900
Truelove, J. K., Klein, R. I., McKee, C. F., et al. 1997, ApJL, 489, L179
Turk, M. J., Smith, B. D., Oishi, J. S., et al. 2011, ApJS, 192, 9
Vázquez-Semadeni, E. 2015, Magnetic Fields in Diffuse Media, 407, 401
Vázquez-Semadeni, E., Gómez, G. C., Jappsen, A. K., et al. 2007, ApJ, 657, 870
Vázquez-Semadeni, E., Banerjee, R., Gómez, G. C., et al. 2011, MNRAS, 414, 2511
Vázquez-Semadeni, E., Colín, P., Gómez, G. C., Ballesteros-Paredes, J., & Watson, A. W. 2010, ApJ, 715, 1302
Vázquez-Semadeni, E., Gazol, A., & Scalo, J. 2000, ApJ, 540, 271
Vázquez-Semadeni, E., Gómez, G. C., Jappsen, A.-K., Ballesteros-Paredes, J., & Klessen, R. S. 2009, ApJ, 707, 1023
Vázquez-Semadeni, E., Ryu, D., Passot, T., González, R. F., & Gazol, A. 2006, ApJ, 643, 245
Vishniac, E. T. 1994, ApJ, 428, 186
Waagan, K. 2009, J. Comput. Phys. 228, 8609
Waagan, K., Federrath, C., & Klingenberg, C. 2011, J. Comput. Phys., 230, 3331
Walch, S., Girichidis, P., Naab, T., et al. 2015, MNRAS, 454, 238
Walch, S., & Naab, T. 2015, MNRAS, 451, 2757
Walder, R., & Folini, D. 2000, Ap& SS, 274, 343
Wolfire, M. G., Hollenbach, D., McKee, C. F., Tielens, A. G. G. M., & Bakes, E. L. O. 1995, ApJ, 443, 152
Zamora-Avilés, M., Vázquez-Semadeni, E., & Colín, P. 2012, ApJ, 751, 77
Zamora-Avilés, M., & Vázquez-Semadeni, E. 2014, ApJ, 793, 84